Electronic Supplementary Material (ESI) for Nanoscale Advances.
This journal is © The Royal Society of Chemistry 2020

Supplementary Information
In-situ laser annealing as pathway for the metal free synthesis of tailored nanographenes

Valeria Milotti,*[1] Manuel Melle-Franco,[2] Ann-Kristin Steiner,[3], Ivan I. Verbitskii,[1] Konstantin Amsharov,[4] and Thomas Pichler[1]

Tailored synthesis of nanographenes, and especially graphene nanoribbons (GNR), has been achieved on metal substrates via a bottom-up approach from organic precursors, which paves the way to their application in nanoelectronics and optoelectronics. Since quantum confinement in nanographenes leads to the creation of peculiar band structures, strongly influenced by their topological characteristics, it is important to be able to exactly engineer them in order to precisely tune their electronic, optical and magnetic properties. However practical application of these materials requires post-synthesis transfer to insulating substrates. Recently, cyclodehydrofluorination of fluorinated organic precursors has been shown to be a promising pathway to achieve metal-free bottom-up synthesis of nanographenes. Here we present how to apply in-situ laser annealing to induce cyclodehydrogenation leading to nanographene formation directly on non-metallic surfaces. In this work, we analyze the changes in the Raman fingerprint of the fluorinated precursor Tetrafluoro-diphenyl-quinquephenyl (TDQ) during the laser annealing process in high vacuum (HV), demonstrating that both heating and photo-induced processes influence the cyclization process. Hence, in-situ laser annealing allows not only to influence chemical reactions, but also to have a fast and contact-free monitoring of the reaction products. Optimization of the laser annealing process adds a new level of control in the tailored synthesis of nanographenes on non-metallic substrates. This is a very promising pathway to unravel the full application potential of nanographenes in general and GNR in particular, enabling a fast optimization of precursor molecules and substrate geometry engineered for specific applications.

[1]Faculty of Physics, University of Vienna, Strudlhofgasse 4, 1090 Vienna, Austria.
[2]CICECO—Aveiro Institute of Materials, Department of Chemistry, University of Aveiro, 3810-193 Aveiro, Portugal.
[3]Department of Organic Chemistry, Friedrich Alexander University Erlangen-Nuremberg, 91058 Erlangen, Germany.
[4]Department of Organic Chemistry, Martin-Luther-Universität Halle Wittenberg, 06108 Halle, Germany.

1 Original data and spectra manipulation

Original data are reported in fig. 1. Fluorescence background from the quartz HV window was subtracted from all spectra. Fluorescence background from the molecule was measured and then subtracted from each spectrum. Spectra were then normalized to the G-line at $\sim$1600cm^{-1}.

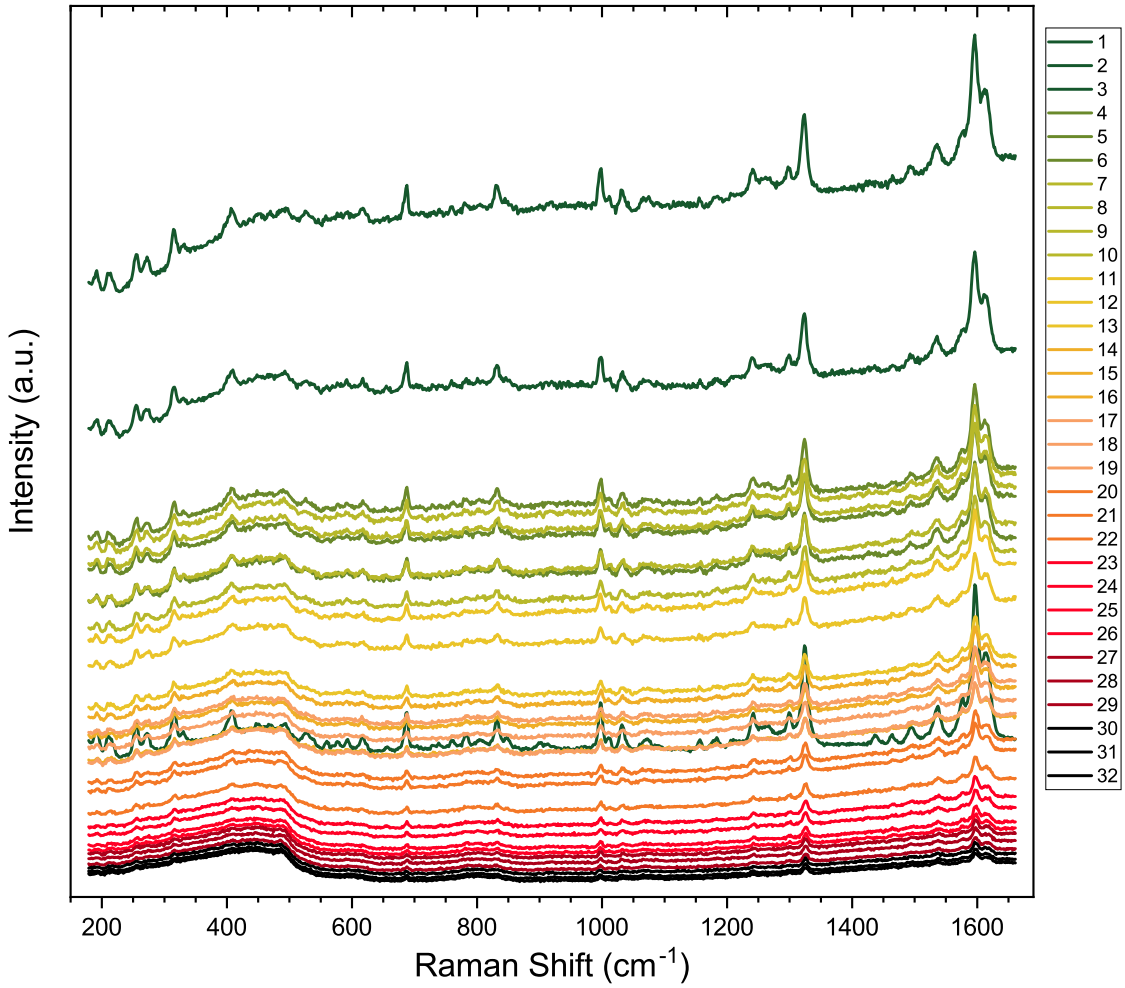

Figure 1 Original data.

2 Comparison between DFT calculations and experimental spectrum of TDQ

As comparison between theory and experiment, peak deconvolution was executed on the G-line (table 1) and the strongest F Raman active modes (table 2), both on the computed spectrum and the experimental 568nm spectrum of TDQ. The peaks were fitted with Voigt profiles. The full width at half maximum (FWHM) of a Voigt profile is estimated to be $w_V = 0.5346 w_L + \sqrt{0.2169 w_L^2 + w_G^2}$, where w_L and w_G are, respectively, the FWHM of the convoluted Lorentzian and Gaussian distributions.[1] As w_G depends on the laser emission linewidth and on the spectrometer resolution, the w_G of the experimental peaks was determined by fitting a Gaussian profile on the laserline measured at 0cm^{-1}.

Center (cm^{-1})		Height (a.u.)		Area (a.u. $\times$ cm^{-1})		FWHM (cm^{-1})	
T	E	T	E	T	E	T	E
1436,32	1437,05	0,21431	0,06626	2,85399	1,35619	8,47851	13,8455
1470,12	1463,65	0,09109	0,05909	1,15058	0,70456	8,04173	3,28575
1489,93	1494,61	0,07921	0,10695	0,99846	2,26327	8,02568	14,2631
1499,56	1519,47	0,34503	0,02251	4,30867	0,55455	7,95648	16,3743
1532,56	1536,22	0,39868	0,21956	4,9809	4,5924	7,99361	14,1156
1581,16	1575,63	0,52559	0,20542	6,71582	4,20047	8,25413	13,8342
1590,63	=	0,26359	=	3,83368	=	9,63832	=
1606,84	1596,82	0,83041	0,93372	10,437	16,7116	8,33816	12,3116
1614,01	1611,78	0,64326	0,33495	6,03812	6,47028	7,00991	1,75384
1622,24	1618,21	0,51351	0,28193	7,03075	4,2217	8,7774	10,5956

Table 1 Peak deconvolution of the G-line of TDQ, comparison between the computed spectrum (T) and experimental spectrum measured at 568nm (E). The peak predicted to be at 1590 was not identifiable in the experimental spectrum.

Center (cm^{-1})		Height (a.u.)		Area (a.u. $\times$ cm^{-1})		FWHM (cm^{-1})	
T	E	T	E	T	E	T	E
255,116	254,726	0,01237	0,20108	0,15853	2,17988	8,15856	8,58354
267,85	272,067	0,00368	0,12742	0,04196	2,11733	7,73693	11,842
303,763	305,819	0,01401	0,0315	0,1701	0,28686	7,88533	7,63797
310,561	315,563	0,02205	0,24073	0,27804	2,76063	8,03409	8,92871
323,72	329,901	0,00838	0,06799	0,10129	0,92728	7,88676	10,1402

Table 2 Peak deconvolution of the strongest Raman active modes with large F displacement in the TDQ spectrum, comparison between the computed spectrum (T) and experimental spectrum measured at 568nm (E).

3 Raman spectrum of target Nanographene

The Raman spectrum of the target nanographene (NG) was acquired with an exciting wavelength of 1064nm (fig. 2). Acquisition at wavelengths in the visible range was hindered by a very strong photoluminescence.

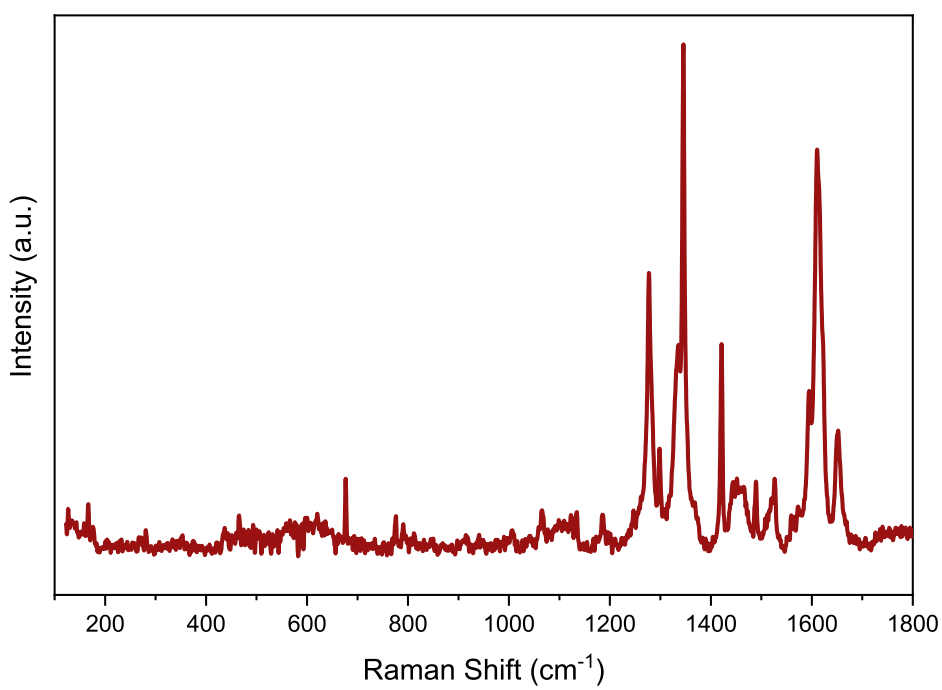

Figure 2 Raman fingerprint of the target NG at exciting wavelength of 1064nm.

4 Temperature calculations

At thermal equilibrium, the ratio between the intensities ϕ_A of the anti-Stokes peak and ϕ_S of the Stokes peak can be approximated to:

$$\frac{\phi_A}{\phi_S} = \left(\frac{\nu_L + \nu_m}{\nu_L - \nu_m}\right)^A \exp\left(-\frac{h\nu_m}{K_B\,T}\right), \qquad A = 3,4 \tag{1}$$

where ν_L is the exciting laser frequency and ν_m is the mode frequency.[2–4] The exponent A depends on the detection method used: according to available literature, $A = 3$ provides more accurate results for photon counting devices such as charge-coupled devices (CCD), while $A = 4$ is better suited for energy-based detection.[5] In our calculations, though our detectors were CCDs, we used both values of A to provide a comparison between the two forms of the equation. From eq. 1, the temperature is:

$$T[K] = \frac{h\nu_m}{K_B}\left[-\log\left(\frac{\phi_A}{\phi_S}\right) + A\log\left(\frac{\nu_L + \nu_m}{\nu_L - \nu_m}\right)\right]^{-1} \tag{2}$$

Results are in tab. 3.

Irradiance (W·cm^{-2})	I_A (a.u.)	I_S (a.u.)	T (K), $A = 3$	T (K), $A = 4$
1.4·10^2	13.3	2336.5	341.5	333.0
3.4·10^2	85.7	4016.2	446.4	432.1
6.0·10^2	17.5	1032.8	424.0	411.1
1.0·10^3	42.0	1028.9	526.3	506.5

Table 3 Experimental data of Stokes and anti-Stokes processes measured with T64000 spectrometer at 532.05nm laser wavelength and temperatures calculated from eq. 2 with $A = 3,4$.

The linewidth of a Raman mode is also dependent on temperature. This dependence is, in the case of a three phonon decay (optical phonon that decays into two acoustic phonons):[4]

$$\Gamma(\nu_m, T) = \Gamma(\nu_m, 0)\left[1 + 2\left(\exp\left(\frac{h\nu_m}{2K_B T}\right) - 1\right)^{-1}\right] \tag{3}$$

Using eqq. 1 and 3 to analyze the Stokes and anti-Stokes processes of the peak at 1326cm^{-1}, we were able to find an estimate for $\Gamma(\nu_m, 0)$ from a non-linear fit of eq. 3 using the temperatures calculated with eq. 5 (fig. 3).

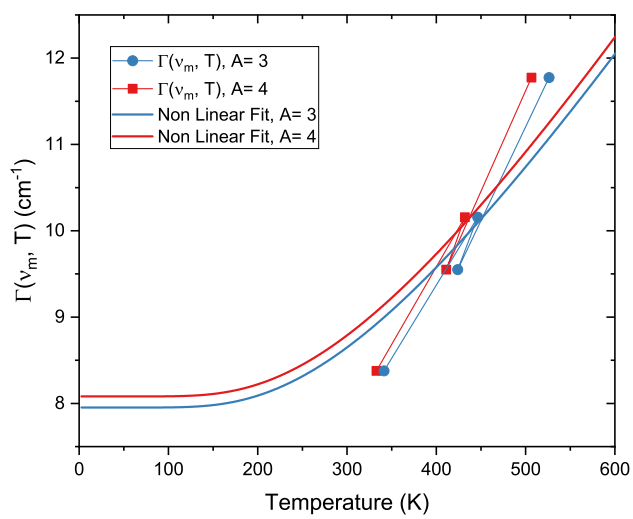

Figure 3 Non-linear fit on (T, $\Gamma(\nu_m, T)$).

The temperatures during laser annealing were then found by inverting eq. 3:

$$T = \frac{h\nu_m}{2K_B}\left(\log\left(\frac{\Gamma(\nu_m, T) + \Gamma(\nu_m, 0)}{\Gamma(\nu_m, T) - \Gamma(\nu_m, 0)}\right)\right)^{-1} \tag{4}$$

A	$\Gamma(\nu_m,0)$ (cm^{-1})	$\sigma_{\Gamma(\nu_m,0)}$ (cm^{-1})
3	7.95283	0.22485
4	8.08142	0.25236

Table 4 $\Gamma(\nu_m,0)$ from non-linear fit of eq. 3.

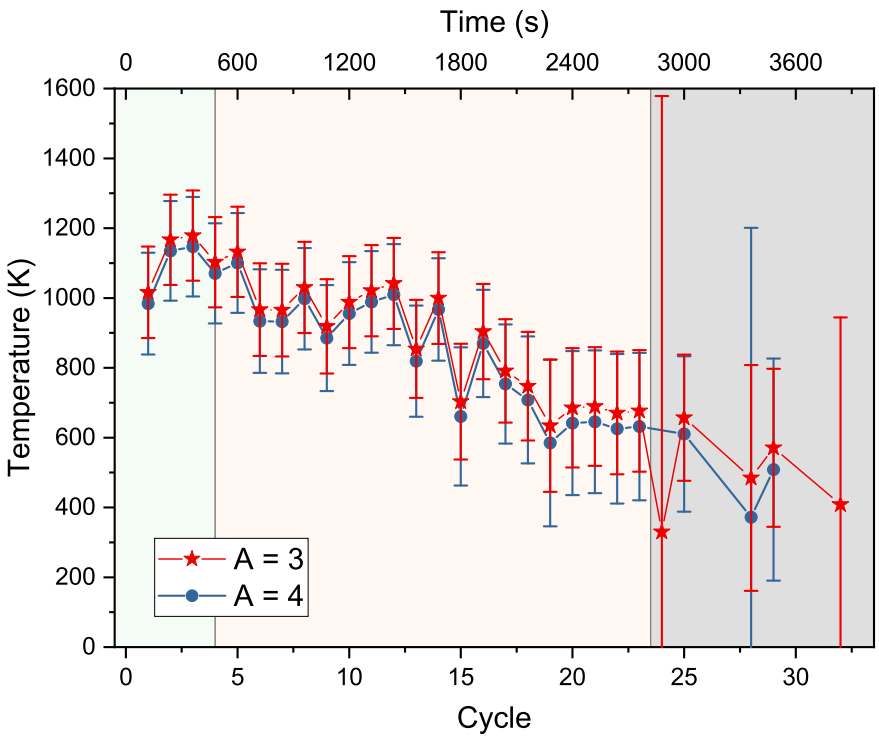

Figure 4 Temperature evolution during laser annealing calculated with eq. 3. The standard deviation was calculated with eq. 5. The temperature increases sharply from room temperature to about 1100K at the beginning of the process and then gradually decreases. The values after cycle 23 (grey shading) are unreliable due to lower signal-to-noise ratios.

and using the Lorentzian width found from fitting a Voigt profile on the peak at 1326cm^{-1} with the program Fityk.[6]. The greatest contribution to the standard deviation on the temperature comes from the error the estimate $\Gamma(\nu_m,0)$, in comparison to which all other contributions are negligible. The standard deviation on the temperature calculated by 4 is thus:

$$\sigma_T = \sqrt{\frac{\partial T}{\partial \Gamma(\nu_m,0)}^2 \sigma^2_{\Gamma(\nu_m,0)}} = \frac{h\nu_m}{K_B}\left(\log^2\left(\frac{\Gamma(\nu_m,T)+\Gamma(\nu_m,0)}{\Gamma(\nu_m,T)-\Gamma(\nu_m,0)}\right)\right)^{-1} \frac{\Gamma(\nu_m,T)}{\Gamma(\nu_m,T)^2-\Gamma(\nu_m,0)^2}\,\sigma_{\Gamma(\nu_m,0)} \tag{5}$$

Results for the temperatures during laser annealing are in tab. 5 and in fig. 4. The exponent $A = 3$ provided temperatures 20K to 50K higher and smaller standard deviations than $A = 4$. The smaller error indicates that $A = 3$ is indeed the better choice for energy based detection. This is in accordance to previous comparisons between the two forms of eq. 1. The temperature of the precursor molecule increased sharply from room temperature to about 1100K during the first two cycles, remained constant until cycle 5 and then decreased slowly. Estimates after cycle 23 are unreliable because of increased fit uncertainty due to decreased signal-to-noise ratio in the Raman spectrum.

	$A=3$		$A=4$	
Cycle	Temperature (K)	σ_T (K)	Temperature (K)	σ_T (K)
1	1016,26	130,93	983,88	145,78
2	1166,80	129,19	1134,98	142,65
3	1178,74	129,25	1146,91	142,66
4	1102,46	129,37	1070,54	143,27
5	1132,09	129,22	1100,23	142,90
6	966,62	132,57	933,76	148,23
7	965,30	132,62	932,43	148,30
8	1030,19	130,47	997,94	145,11
9	918,81	135,17	885,23	151,93
10	988,11	131,79	955,48	147,07
11	1021,03	130,76	988,69	145,54
12	1041,80	130,28	1009,61	144,80
13	854,08	140,42	819,02	159,38
14	999,76	131,47	967,23	146,58
15	703,12	165,89	660,72	197,80
16	903,79	136,29	869,90	153,50
17	790,98	148,14	753,75	170,55
18	747,42	155,65	708,03	181,78
19	634,36	189,60	584,65	238,81
20	685,58	170,98	641,66	206,07
21	689,01	169,98	645,40	204,42
22	670,74	175,88	625,33	214,27
23	676,54	174,01	631,70	211,09
24	330,20	1248,19	–	–
25	657,24	180,69	610,36	222,58
26	–	–	–	–
27	–	–	–	–
28	484,54	323,51	372,14	828,69
29	570,83	226,30	508,52	317,92
30	–	–	–	–
31	–	–	–	–
32	408,17	536,02	–	–

Table 5 Temperatures and standard deviations calculated with eqq. 4 and 5

5 Analysis of intensity of peak at 1326cm^{-1}

Intensity decay can be separated at cycle 4 (480s) into two well defined regimes of exponential decrease. Each regime can be modeled by: $I = e^{-\lambda t}$. Calculated λ are in tab. 6. Values are given for time expressed either in cycles or in seconds.

Regime	λ (cycle^{-1})	$\sigma\lambda$ (cycle^{-1})	λ (s^{-1})	$\sigma\lambda$ (s^{-1})
Evaporation	796.85	0.04	$6.64 \cdot 10^{-2}$	$3.01 \cdot 10^{-4}$
Decomposition	744.47	0.03	$6.20 \cdot 10^{-2}$	$2.46 \cdot 10^{-4}$

Table 6 Decay constants from fit.

Notes and references

[1] J. Olivero and R. Longbothum, *Journal of Quantitative Spectroscopy and Radiative Transfer*, 1977, **17**, 233–236.

[2] M. Malyj and J. E. Griffiths, *Applied Spectroscopy*, 1983, **37**, 315–333.

[3] B. J. Kip and R. J. Meier, *Applied Spectroscopy*, 1990, **44**, 707–711.

[4] H. Kuzmany, *Solid-State Spectroscopy*, Springer Berlin Heidelberg, 2009.

[5] J. J. Gallardo, J. Navas, D. Zorrilla, R. Alcántara, D. Valor, C. Fernández-Lorenzo and J. Martín-Calleja, *Applied Spectroscopy*, 2016, **70**, 1128–1136.

[6] M. Wojdyr, *Journal of Applied Crystallography*, 2010, **43**, 1126–1128.